IOP Publishing Physics in Medicine and Biology

Phys. Med. Biol. **52** (2007) 5393–5414 doi:10.1088/0031-9155/52/17/020

A new scheme for view-dependent data differentiation in fan-beam and cone-beam computed tomography

Frédéric Noo[1], Stefan Hoppe[2], Frank Dennerlein[1], Günter Lauritsch[3] and Joachim Hornegger[2]

[1] UCAIR, Department of Radiology, University of Utah, UT, USA
[2] Institute of Pattern Recognition, University of Erlangen-Nuremberg, Germany
[3] Siemens AG, Medical Solutions, Forchheim, Germany

E-mail: noo@ucair.med.utah.edu

Received 23 March 2007, in final form 25 July 2007
Published 21 August 2007
Online at stacks.iop.org/PMB/52/5393

Abstract

In computed tomography, analytical fan-beam (FB) and cone-beam (CB) image reconstruction often involves a view-dependent data differentiation. The implementation of this differentiation step is critical in terms of resolution and image quality. In this work, we present a new differentiation scheme that is robust to changes in the data acquisition geometry and to coarse view sampling. Our scheme was compared to two previously suggested methods, which we call the direct scheme and the chain-rule scheme. Image reconstructions were performed from computer-simulated data of the Shepp–Logan phantom, the FORBILD thorax phantom and a modified FORBILD head phantom. For FB reconstruction, we investigated three acquisition geometries: a circular, an ellipse-shaped and a square-shaped trajectory. For CB reconstruction, the circle-plus-line trajectory was considered. Image comparison showed that the new scheme performs consistently well when varying the scenario, in both FB and CB geometry, unlike the other two schemes.

1. Introduction

A specific view-dependent data differentiation has become a common processing step in analytical image reconstruction from fan-beam (FB) and cone-beam (CB) projections in x-ray computed tomography (CT). See e.g., Katsevich (2003), Noo *et al* (2002), Chen (2003a), Zou and Pan (2004), Yu and Wang (2004, 2005), Bontus *et al* (2005), Sidky *et al* (2005) and Pack and Noo (2005). This differentiation step, which we describe below, is often regarded as a non-desired feature, or more specifically as a feature that is bound to yield unwanted resolution loss and discretization errors. Hence, several authors have suggested to modify the reconstruction formula using integration by parts, in such a way as to eliminate the differentiation step (e.g., Katsevich (2002), Chen (2003b), Sidky *et al* (2005), Katsevich *et al* (2006), Yang *et al* (2006)).

This approach is effective in that clear improvements in resolution and image quality have been reported (see, e.g., Katsevich *et al* (2003) and Yang *et al* (2006)). Unfortunately, for the filtered-backprojection methods, the integration by parts generally renders the reconstruction formula much more demanding in terms of computational effort; for example, more than one non-local filtering operation may be needed after integration by parts, and there may be the additional request to backproject each filtering result with a different weight. Given this weakness of the integration by parts, we decided to revisit the problem of performing the view-dependent differentiation from discrete data. Doing so, we found a new differentiation scheme, which we present here. We believe this scheme is more robust than previously proposed schemes, and we demonstrate this to be at least the case in two geometries: first, the reconstruction from FB projections measured on a convex source trajectory, and second, the reconstruction from CB data measured on a circle-plus-line trajectory.

We now describe the view-dependent data differentiation step we are concerned with. First, let $f(\underline{x})$ be the x-ray linear attenuation coefficient to be reconstructed, and let $g(\lambda, \underline{\alpha})$ be the FB or CB data from which $f(\underline{x})$ needs to be reconstructed. In this notation, λ is a scalar that specifies the position of the x-ray source on a curve, $\underline{\alpha}$ is a unit vector, and $g(\lambda, \underline{\alpha})$ is the integral of $f(\underline{x})$ along the half-line of direction $\underline{\alpha}$ that starts from the source position at λ. In a circular or helical data acquisition geometry, λ usually corresponds to the rotation angle of the source–detector assembly. By definition, a reconstruction formula is the expression of an approximation of $f(\underline{x})$ in terms of the data $g(\lambda, \underline{\alpha})$. To achieve an accurate approximation, many formulas nowadays require the computation of

$$g_D(\lambda, \underline{\alpha}) = \frac{\partial}{\partial \lambda} g(\lambda, \underline{\alpha}) \bigg|_{\underline{\alpha}\ \text{fixed}} = \lim_{\varepsilon \to 0} \frac{g(\lambda + \varepsilon, \underline{\alpha}) - g(\lambda - \varepsilon, \underline{\alpha})}{2\varepsilon} \tag{1}$$

as a first data-processing step. This computation defines the differentiation step this paper focuses on. Basically, we need to differentiate $g(\lambda, \underline{\alpha})$ with respect to λ while keeping the ray direction $\underline{\alpha}$ fixed. In practice, this operation is difficult to implement accurately because the sampled values of $\underline{\alpha}$ change with λ, as they are specified by the detector sampling and the position of the source and detector relative to each other. Furthermore, the sampling in λ is often coarser than the sampling on the detector.

The paper is organized in five sections. In section 2, we first review two differentiation schemes that have been previously suggested for the implementation of (1), then we describe our new scheme. After that, we compare in sections 3 and 4 reconstruction results that have been obtained from various sets of computer-simulated data using these three schemes. This comparison aims at demonstrating the robustness of the new scheme. Section 3 addresses the reconstruction from fan-beam data on three convex source trajectories, while section 4 outlines the reconstruction from cone-beam data on a circle-plus-line source trajectory. At the end, section 5 summarizes the content of the paper and discusses the various related aspects.

2. View-dependent differentiation

In this section, we review two schemes that have previously been suggested for the implementation of (1), then present our new scheme. To simplify the discussion, some hypotheses are made on the data acquisition geometry, and these hypotheses are given first.

2.1. Geometric assumptions

Throughout this work, the source trajectory is viewed either as a single curve or the union of a finite number of curves. We assume that the projections are measured with a fixed sampling

distance in λ on each of these curves. However, we allow this distance to vary from one curve to another.

For the computation of $g_D(\lambda, \underline{\alpha})$ in equation (1), there is nothing that fundamentally changes from one curve that forms the source trajectory to another, so we can focus the discussion in this section on any one of these curves. We write the sampling distance and the number of projections on the selected curve as $\Delta\lambda$ and N_λ, respectively, and we use $\lambda_i = \lambda_0 + i\Delta\lambda$ to specify the position of the projections measured on this curve. In this notation, λ_0 defines the source position for the first projection, and i is an integer that runs from 0 to $N_\lambda - 1$.

Some hypotheses are also made on the detector geometry: we assume the detector is flat and we assume the detector pixels fit perfectly on a Cartesian grid of points in the detector plane. The coordinates used to define this grid are denoted by u and v and are such that the point $(u, v) = (0, 0)$ corresponds to the orthogonal projection of the source position onto the detector plane. The points on which the detector pixels are centered have $u_j = u_0 + j\Delta u$ and $v_k = v_0 + k\Delta v$ for coordinates, with $j = 0, \ldots, N_u - 1$ and $k = 0, \ldots, N_v - 1$. We call N_u the number of detector columns and N_v the number of detector rows. In our notation, changing (u_0, v_0) amounts to physically translating the detector while keeping the detector plane unchanged relative to the source position. Note that in FB geometry, there is only one row of detector pixels, and therefore $N_v = 1$. In this case, v gives the direction along which the detector thickness is measured, while u gives the direction along which the detector pixels are aligned.

Let $g_m(\lambda, u, v)$ be the integral of $f(\underline{x})$ along the half-line that connects the source position at λ to the point of coordinates (u, v) in the detector plane. The quantities we have introduced allow the measured data to be seen as a sampling of $g_m(\lambda, u, v)$ with the samples being $g_m(\lambda_i, u_j, v_k)$. To link $g_m(\lambda, u, v)$ to the expression $g(\lambda, \underline{\alpha})$ that was used to describe the data in the introduction, we introduce a distance $D(\lambda)$ and three unit orthogonal vectors, $\underline{e}_u(\lambda)$, $\underline{e}_v(\lambda)$ and $\underline{e}_w(\lambda) = \underline{e}_u(\lambda) \times \underline{e}_v(\lambda)$. As emphasized, these four quantities may each depend on λ. Vector $\underline{e}_w(\lambda)$ is orthogonal to the detector plane and points toward the source position, which is pictured at distance $D(\lambda)$ from this plane. Thus, $\underline{e}_u(\lambda)$ and $\underline{e}_v(\lambda)$ are always parallel to the detector plane, and we let them define the axes along which the coordinates u and v are measured. Under these conditions,

$$g_m(\lambda, u, v) = g(\lambda, \hat{\underline{\alpha}}) \tag{2}$$

with

$$\hat{\underline{\alpha}} = \frac{u\underline{e}_u(\lambda) + v\underline{e}_v(\lambda) - D(\lambda)e_w(\lambda)}{\sqrt{u^2 + v^2 + (D(\lambda))^2}}. \tag{3}$$

Consequently,

$$\begin{cases} u = -D(\lambda)\dfrac{\hat{\underline{\alpha}} \cdot \underline{e}_u(\lambda)}{\hat{\underline{\alpha}} \cdot \underline{e}_w(\lambda)} \\ v = -D(\lambda)\dfrac{\hat{\underline{\alpha}} \cdot \underline{e}_v(\lambda)}{\hat{\underline{\alpha}} \cdot \underline{e}_w(\lambda)}. \end{cases} \tag{4}$$

See figure 1. In particular, we have

$$g_m(\lambda_i, u_j, v_k) = g(\lambda, \underline{\alpha}_{i,j,k}) \tag{5}$$

with

$$\underline{\alpha}_{i,j,k} = \frac{u_j\underline{e}_u(\lambda_i) + v_k\underline{e}_v(\lambda_i) - D(\lambda_i)\underline{e}_w(\lambda_i)}{\sqrt{(u_j)^2 + (v_k)^2 + (D(\lambda_i))^2}}. \tag{6}$$

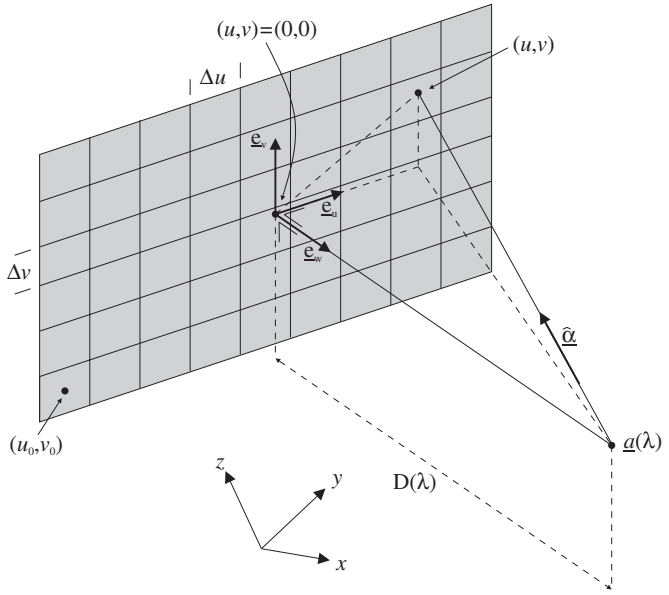

Figure 1. Data acquisition geometry with a flat panel detector. See the text in section 2.1 for details.

Conversely, if the line of direction $\underline{\alpha}$ through the source position at λ hits the detector in the direction of $\underline{\alpha}$, then

$$g(\lambda, \underline{\alpha}) = g_m(\lambda, \hat{u}, \hat{v}) \tag{7}$$

with

$$\begin{cases} \hat{u} = -D(\lambda)\dfrac{\underline{\alpha} \cdot \underline{e}_u(\lambda)}{\underline{\alpha} \cdot \underline{e}_w(\lambda)} \\ \hat{v} = -D(\lambda)\dfrac{\underline{\alpha} \cdot \underline{e}_v(\lambda)}{\underline{\alpha} \cdot \underline{e}_w(\lambda)}. \end{cases} \tag{8}$$

The differentiation step in equation (1) converts $g_m(\lambda, u, v)$ into another function $g'_m(\lambda, u, v)$ such that

$$g'_m(\lambda, u, v) = g_D(\lambda, \hat{\underline{\alpha}}) \tag{9}$$

with $\hat{\underline{\alpha}}$ given by equation (3). Likewise, for any $\underline{\alpha}$ that points toward the detector plane

$$g_D(\lambda, \underline{\alpha}) = g'_m(\lambda, \hat{u}, \hat{v}) \tag{10}$$

with $\hat{u}$ and $\hat{v}$ defined in (8).

2.2. The direct scheme

This scheme amounts to a direct discretization of (1), in the form

$$g_D(\lambda + \Delta\lambda/2, \underline{\alpha}) \simeq \frac{g(\lambda + \Delta\lambda, \underline{\alpha}) - g(\lambda, \underline{\alpha})}{\Delta\lambda}. \tag{11}$$

Thus, each measured projection is differentiated from the previous one while ensuring the ray direction remains fixed, and the outcome is placed at the mid-position in λ.

Formula (11) is implemented as the computation of $g'_m(\lambda, u, v)$ at $(\lambda_{i+1/2}, u_j, v_k)$ according to the formula

$$g'_m(\lambda_{i+1/2}, u_j, v_k) \simeq \frac{g(\lambda_{i+1}, \underline{\alpha}_{i+1/2,j,k}) - g(\lambda_i, \underline{\alpha}_{i+1/2,j,k})}{\Delta\lambda} \tag{12}$$

where $\underline{\alpha}_{i+1/2,j,k}$ is the result of equation (6) with λ_i replaced by $\lambda_{i+1/2} = \lambda_i + \Delta\lambda/2$. Of course, in general, neither of the two terms in the numerator of (12) is part of the measurements. To solve this issue, equation (12) is applied using an approximation of these terms based on equation (7) and bilinear interpolation. For example, to estimate $g(\lambda_{i+1}, \underline{\alpha}_{i+1/2,j,k})$, we apply equation (8) using λ_{i+1} for λ and $\underline{\alpha}_{i+1/2,j,k}$ for $\underline{\alpha}$. The outcome of this application is the coordinates of a point in the detector plane that depend on the indices i, j and k and may be denoted as

$$\begin{cases} \hat{u}_{i,j,k} = -D(\lambda_{i+1}) \dfrac{\underline{\alpha}_{i+1/2,j,k} \cdot \underline{e}_u(\lambda_{i+1})}{\underline{\alpha}_{i+1/2,j,k} \cdot \underline{e}_w(\lambda_{i+1})} \\ \hat{v}_{i,j,k} = -D(\lambda_{i+1}) \dfrac{\underline{\alpha}_{i+1/2,j,k} \cdot \underline{e}_v(\lambda_{i+1})}{\underline{\alpha}_{i+1/2,j,k} \cdot \underline{e}_w(\lambda_{i+1})}. \end{cases} \tag{13}$$

The value of $g_m(\lambda_{i+1}, \underline{\alpha}_{i+1/2,j,k})$ is estimated from bilinear interpolation of the four detector pixel values that are closest to $(\hat{u}_{i,j,k}, \hat{v}_{i,j,k})$ in the projection at λ_{i+1}.

2.3. The chain-rule scheme

Here, we use (9) in combination with (1) and (2) to write

$$g'_m(\lambda, u, v) = g_D(\lambda, \underline{\hat{\alpha}}) = \frac{\partial}{\partial\lambda} g(\lambda, \underline{\hat{\alpha}})\bigg|_{\underline{\hat{\alpha}}\ \text{fixed}} = \frac{\partial}{\partial\lambda} g_m(\lambda, u, v)\bigg|_{\underline{\hat{\alpha}}\ \text{fixed}}. \tag{14}$$

Then, we apply the chain rule recalling that u and v are tied to $\underline{\hat{\alpha}}$ through equation (4). The outcome is

$$g'_m(\lambda, u, v) = \left(\frac{\partial g_m}{\partial\lambda}\right)(\lambda, u, v) + w_0(u, v)\left(\frac{\partial g_m}{\partial u}\right)(\lambda, u, v) + w_1(u, v)\left(\frac{\partial g_m}{\partial v}\right)(\lambda, u, v) \tag{15}$$

where

$$w_0(u, v) = \frac{\partial u}{\partial\lambda}\bigg|_{\underline{\hat{\alpha}}\ \text{fixed}} \tag{16}$$

and

$$w_1(u, v) = \frac{\partial v}{\partial\lambda}\bigg|_{\underline{\hat{\alpha}}\ \text{fixed}}. \tag{17}$$

To get practical expressions for $w_0(u, v)$ and $w_1(u, v)$, we replace u and v in (16) and (17) by their expression from (4), we apply the differentiation in λ at fixed $\underline{\hat{\alpha}}$, and then replace $\underline{\hat{\alpha}}$ by its expression from (3). Recalling that $\underline{e}'_u(\lambda) \cdot \underline{e}_u(\lambda) = 0$, $\underline{e}'_w(\lambda) \cdot \underline{e}_w(\lambda) = 0$ and $\underline{e}_w(\lambda) \cdot \underline{e}'_u(\lambda) = -\underline{e}_u(\lambda) \cdot \underline{e}'_w(\lambda)$ because $\underline{e}_u(\lambda)$ and $\underline{e}_w(\lambda)$ are unit orthogonal vectors, we get

$$w_0(u, v) = \frac{u D'(\lambda)}{D(\lambda)} + \frac{u^2 + D^2}{D}\underline{e}_u(\lambda) \cdot \underline{e}'_w(\lambda) + v\underline{e}_v(\lambda) \cdot \left(\underline{e}'_u(\lambda) + \frac{u}{D}\underline{e}'_w(\lambda)\right) \tag{18}$$

where the prime refers to taking a derivative in λ; for example, $\underline{e}'_w(\lambda) = \mathrm{d}\underline{e}_w(\lambda)/\mathrm{d}\lambda$. Similarly,

$$w_1(u, v) = \frac{v D'(\lambda)}{D(\lambda)} + \frac{v^2 + D^2}{D}\underline{e}_v(\lambda) \cdot \underline{e}'_w(\lambda) + u\underline{e}_u(\lambda) \cdot \left(\underline{e}'_v(\lambda) + \frac{v}{D}\underline{e}'_w(\lambda)\right). \tag{19}$$

Two ways of implementing (15) are considered in this paper. The first way, called here *the blended chain-rule scheme*, consists in computing each derivative in (15) using an average of differences of consecutive values, defined so that the final result is an estimate of $g'_m(\lambda, u, v)$ at $(\lambda_{i+1/2}, u_{j+1/2}, v_{k+1/2})$. The detailed formula is

$$\begin{aligned} g'_m(\lambda_{i+1/2}, u_{j+1/2}, v_{k+1/2}) \simeq{}& \frac{1}{\Delta\lambda}\sum_{j'=j}^{j+1}\sum_{k'=k}^{k+1}(g_m(\lambda_{i+1}, u_{j'}, v_{k'}) - g_m(\lambda_i, u_{j'}, v_{k'})) \\ &+ \frac{w_0(u_{j+1/2}, v_{k+1/2})}{\Delta u}\sum_{i'=i}^{i+1}\sum_{k'=k}^{k+1}(g_m(\lambda_{i'}, u_{j+1}, v_{k'}) - g_m(\lambda_{i'}, u_j, v_{k'})) \\ &+ \frac{w_1(u_{j+1/2}, v_{k+1/2})}{\Delta v}\sum_{i'=i}^{i+1}\sum_{j'=j}^{j+1}(g_m(\lambda_{i'}, u_{j'}, v_{k+1}) - g_m(\lambda_{i'}, u_{j'}, v_k)). \end{aligned} \tag{20}$$

Note that without the averaging process, the computation of each term in (15) through the difference of consecutive values would yield an estimate of each term at a different location, thus complicating the filtering and backprojection steps that are typically applied to the data after computation of g'_m. Formula (20) was identified in Noo *et al* (2003) as a preferred approach for helical CB reconstruction using Katsevich's formula (Katsevich 2004a).

The second way we consider here for the implementation of (15) is called the *split chain-rule scheme*. This scheme acknowledges that the sampling in λ is often coarser than the sampling in (u, v), and thus aims at limiting losses in λ through splitting off the first term in (15) from the other two terms. More specifically, we compute on one hand

$$g'_{m,1}(\lambda_{i+1/2}, u_j, v_k) \simeq \frac{1}{\Delta\lambda}(g_m(\lambda_{i+1}, u_j, v_k) - g_m(\lambda_i, u_j, v_k)) \tag{21}$$

as an approximation of the first term in (15), and on the other hand we compute

$$\begin{aligned} g'_{m,2}(\lambda_i, u_{j+1/2}, v_{k+1/2}) \simeq{}& \frac{w_0(u_{j+1/2}, v_{k+1/2})}{\Delta u}\sum_{k'=k}^{k+1}(g_m(\lambda_i, u_{j+1}, v_{k'}) - g_m(\lambda_i, u_j, v_{k'})) \\ &+ \frac{w_1(u_{j+1/2}, v_{k+1/2})}{\Delta v}\sum_{j'=j}^{j+1}(g_m(\lambda_i, u_{j'}, v_{k+1}) - g_m(\lambda_i, u_{j'}, v_k)) \end{aligned} \tag{22}$$

as an approximation of the sum of the other two terms in (15). Using this scheme allows a strong control of resolution losses in λ. However, observe that it causes the computational effort to be doubled for most reconstruction methods because $g'_{m,1}$ and $g'_{m,2}$, are not computed on the same grid and thus need to be filtered and backprojected separately whenever such steps are required.

2.4. The new scheme

Like the direct scheme, this scheme amounts to a direct discretization of (1), but this time in the form

$$g'(\lambda, \underline{\alpha}) \simeq \frac{g(\lambda + \varepsilon\Delta\lambda, \underline{\alpha}) - g(\lambda - \varepsilon\Delta\lambda, \underline{\alpha})}{2\varepsilon\Delta\lambda} \tag{23}$$

where ε is a free parameter between 0 and 1; more specifically, $0 < \varepsilon \leqslant 1$. Note that no shift is applied anymore in λ. Note also, from the form of (23), that ε may be interpreted as a resolution-control parameter.

To implement (23), we need to define a method to estimate from the sampled data each term that appears in its numerator. In the direct scheme, this task was easy because each term

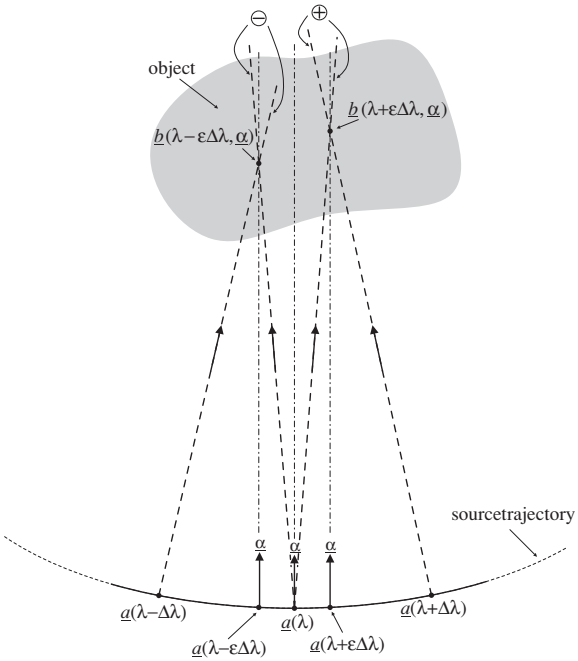

Figure 2. The new scheme for data differentiation. We first approximate the value of $g(\lambda+\varepsilon\Delta\lambda, \underline{\alpha})$ by a linear combination of the projection values at λ and $\lambda+\Delta\lambda$ along the lines that contain $\underline{b}(\lambda+\varepsilon\Delta\lambda, \underline{\alpha})$ (see the lines labeled with the $\oplus$ sign). Next, we approximate the value of $g(\lambda-\varepsilon\Delta\lambda, \underline{\alpha})$ in a similar way, but from the lines labeled with the $\ominus$ sign. From there, $g_D(\lambda, \underline{\alpha})$ is obtained by differentiation of the approximations obtained for $g(\lambda+\varepsilon\Delta\lambda, \underline{\alpha})$ and $g(\lambda-\varepsilon\Delta\lambda, \underline{\alpha})$.

in the numerator of (11) could be forced to correspond to one sampled source position, as shown in (12). This approach is no longer possible here as ε is a free parameter.

To estimate the two terms in the numerator of (23), we introduce a function $\underline{b}(\lambda, \underline{\alpha})$ that gives the position of a point-of-interest along the line of direction $\underline{\alpha}$ through $\underline{a}(\lambda)$, the source position at λ. Then, we approximate the first term, $g(\lambda+\varepsilon\Delta\lambda, \underline{\alpha})$, as a linear combination of the projection values at λ and $\lambda+\Delta\lambda$ along the lines that contain $\underline{b}(\lambda+\varepsilon\Delta\lambda, \underline{\alpha})$. See figure 2. In a detailed form, we carry out the following approximation:

$$g(\lambda+\varepsilon\Delta\lambda, \underline{\alpha}) \simeq (1-\varepsilon)g\left(\lambda, \frac{\underline{b}(\lambda+\varepsilon\Delta\lambda, \underline{\alpha}) - \underline{a}(\lambda)}{\|\underline{b}(\lambda+\varepsilon\Delta\lambda, \underline{\alpha}) - \underline{a}(\lambda)\|}\right) + \varepsilon g\left(\lambda+\Delta\lambda, \frac{\underline{b}(\lambda+\varepsilon\Delta\lambda, \underline{\alpha}) - \underline{a}(\lambda+\Delta\lambda)}{\|\underline{b}(\lambda+\varepsilon\Delta\lambda, \underline{\alpha}) - \underline{a}(\lambda+\Delta\lambda)\|}\right). \tag{24}$$

The second term, $g(\lambda-\varepsilon\Delta\lambda, \underline{\alpha})$, is obtained similarly, and this amounts simply to computing the right-hand side of (24) with $\Delta\lambda$ replaced by $-\Delta\lambda$. If λ is chosen as a sampled source position, then each value of g on the right-hand-side of (24) can be computed from the measured data using bilinear interpolation in (u, v), in the same way as with equation (13) in section 2.2.

The new scheme is defined as the computation of $g'_m(\lambda_i, u_{j+1/2}, v_{k+1/2})$ following equations (23) and (24). More specifically, we compute

$$g'(\lambda_i, u_{j+1/2}, v_{k+1/2}) \simeq \frac{g(\lambda_i+\varepsilon\Delta\lambda, \underline{\alpha}_{i,j+1/2,k+1/2}) - g(\lambda_i-\varepsilon\Delta\lambda, \underline{\alpha}_{i,j+1/2,k+1/2})}{2\varepsilon\Delta\lambda} \tag{25}$$

where the two terms in the numerator are each obtained using (24) with bilinear interpolation in (u, v). The half-pixel shift in u and v is another feature that distinguishes the new scheme from the direct scheme. We apply this shift so that the scheme closely resembles a difference between consecutive detector samples when ε tends to zero and $\underline{a}(\lambda)$ is far from the object. We found through experimental evaluations that this shift indeed carries with it a significant gain in resolution.

At this stage, the new scheme is not yet completely explained, as no specific definition was given for $\underline{b}(\lambda, \underline{\alpha})$, which we called the point-of-interest. We would like to picture $\underline{b}(\lambda, \underline{\alpha})$ as the center of mass of the object density along the line of direction $\underline{\alpha}$ through $\underline{a}(\lambda)$. This would in some ways optimize the accuracy of (24). However, such a definition is not practical since the object density is *a priori* unknown. To handle this issue, an axis, say $\mathcal{L}$, around which the object is known to be globally centered is selected. Then, $\underline{b}(\lambda, \underline{\alpha})$ is defined as the point on the line of direction $\underline{\alpha}$ through $\underline{a}(\lambda)$ that is closest to $\mathcal{L}$. If $\underline{x}_0$ defines an arbitrary point on $\mathcal{L}$ and $\underline{n}$ is the direction of $\mathcal{L}$, then it can be shown that

$$\underline{b}(\lambda, \underline{\alpha}) = \underline{a}(\lambda) + \frac{(\underline{x}_0 - \underline{a}(\lambda)) \cdot (\underline{\alpha} - (\underline{\alpha} \cdot \underline{n})\underline{n})}{1 - (\underline{\alpha} \cdot \underline{n})^2} \underline{\alpha}. \tag{26}$$

3. Evaluation in fan-beam geometry

We have performed evaluations in fan-beam geometry using a convex curve for the source trajectory. The object was always inside the convex hull of this trajectory. Consequently, each line passing through the object intersected the source trajectory exactly twice, so that the redundancy in the data could be easily handled through giving a weight of $1/2$ to each line integral. We considered three specific trajectories: a circle, an ellipse-shaped trajectory, and a square-shaped trajectory. And we considered two mathematical phantoms: the Shepp–Logan phantom and the FORBILD thorax phantom. For the Shepp–Logan phantom, every fan-beam data sample was computed as a simple line integral. For the thorax phantom, every fan-beam data sample was obtained using a combination of line integrals to model physical resolution-degradating factors, as detailed in section 3.6. In either case, analytic formulas were used for the computation of line integrals.

3.1. Data acquisition geometry

The source position $\underline{a}(\lambda)$ was defined with λ varying in a given domain called Λ. The object was globally centered on the axis orthogonal to the source-trajectory plane through the origin, and this axis was chosen as $\mathcal{L}$ for the computation of $\underline{b}(\lambda, \underline{\alpha})$ in equation (26). Furthermore, D was assumed to be independent of λ, and vectors $\underline{e}_u(\lambda)$ and $\underline{e}_w(\lambda)$ were selected as follows:

$$\begin{cases} \underline{e}_u(\lambda) = \dfrac{\underline{a}'(\lambda)}{\|\underline{a}'(\lambda)\|} \\ \underline{e}_w(\lambda) = \dfrac{\underline{a}(\lambda) - \big(\underline{a}(\lambda) \cdot \underline{e}_u(\lambda)\big)\, \underline{e}_u(\lambda)}{\big\|\underline{a}(\lambda) - \big(\underline{a}(\lambda) \cdot \underline{e}_u(\lambda)\big)\, \underline{e}_u(\lambda)\big\|}. \end{cases} \tag{27}$$

In this particular geometry, the data are $g_m(\lambda, u)$, and from equation (15)

$$g'_m(\lambda, u) = \left(\frac{\partial g_m}{\partial \lambda}\right)(\lambda, u) + \frac{u^2 + D^2}{D} \underline{e}_u(\lambda) \cdot \underline{e}'_w(\lambda) \left(\frac{\partial g_m}{\partial u}\right)(\lambda, u). \tag{28}$$

3.2. The reconstruction formula

For reconstruction, we used the fan-beam filtered-backprojection (FBP) formula that was suggested in Noo *et al* (2002). This formula yields the following regularized version of $f(\underline{x})$:

$$\hat{f}(\underline{x}) = \frac{1}{4\pi} \int_{\Lambda} \frac{\mathrm{d}\lambda}{(\underline{a}(\lambda) - \underline{x}) \cdot \underline{e}_w(\lambda)} \int_{-\infty}^{\infty} \mathrm{d}u \, h_{\mathrm{H}}(u^*(\lambda, \underline{x}) - u) \frac{D g'_m(\lambda, u)}{\sqrt{D^2 + u^2}} \tag{29}$$

where

$$u^*(\lambda, \underline{x}) = -D \frac{(\underline{x} - \underline{a}(\lambda)) \cdot \underline{e}_u(\lambda)}{(\underline{x} - \underline{a}(\lambda)) \cdot \underline{e}_w(\lambda)} \tag{30}$$

and where $h_{\mathrm{H}}(u)$ is an apodized version of the Hilbert transform kernel, namely

$$h_{\mathrm{H}}(u) = \int_{-\frac{1}{2\Delta u}}^{\frac{1}{2\Delta u}} -\mathrm{i}\,\mathrm{sign}(\nu)\, \mathrm{e}^{\mathrm{i}2\pi\nu t} \, \mathrm{d}t = \frac{1 - \cos(\pi u/\Delta u)}{\pi u}. \tag{31}$$

By construction, $\hat{f}(\underline{x})$ converges toward $f(\underline{x})$ in L^2 norm (i.e., in the root mean square difference) when Δu converges toward zero, provided $f(\underline{x})$ is a square-integrable function.

The implementation of (29) was performed using the fast Fourier transform (FFT) to compute the convolution in u, and using the trapezoidal rule (Johnson and Riess 1982) with linear interpolation in u for discretization of the backprojection integral (i.e., the integral in λ). When computing the convolution in u, the samples were shifted by $(\Delta u)/2$ in u; doing so was previously shown to be useful in terms of resolution and aliasing errors (Noo *et al* 2003).

3.3. The circular trajectory

The first trajectory we considered was a circle of radius $R = 300$ mm centered on the origin. We selected λ as the polar angle, and thus $\underline{a}(\lambda) = [R\cos\lambda, R\sin\lambda]$ with $\Lambda = [0, 2\pi)$. From (27), this choice yields $\underline{e}_u(\lambda) = [-\sin\lambda, \cos\lambda]$ and $\underline{e}_w(\lambda) = [\cos\lambda, \sin\lambda]$, so that equation (28) becomes

$$g'_m(\lambda, u) = \left(\frac{\partial g_m}{\partial \lambda}\right)(\lambda, u) + \frac{u^2 + D^2}{D} \left(\frac{\partial g_m}{\partial u}\right)(\lambda, u). \tag{32}$$

Reconstructions of the conventional Shepp–Logan phantom (Kak and Slaney 1988) were performed in this geometry, from 501 projections defined with $\Delta\lambda = 2\pi/501$, $\Delta u = 1$ mm and $D = 300$ mm, and using $\varepsilon = 0.001$ for the new scheme. Figure 3 shows the reconstruction of the whole phantom on a grid of 512×512 square pixels of side 0.4 mm, while figure 4 shows a profile through a reconstruction that was zoomed on the three little ellipses in the lower part of the phantom. The pixel width for the zoom was 0.1 mm, and the profile was taken along the line going through the center of the ellipses. We see that in this geometry (i) the direct scheme causes a dramatic loss in resolution compared to the other schemes, (ii) the split chain-rule scheme offers some improvement over the blended chain-rule scheme, and (iii) for the selected ε, the new scheme performs as well as the split chain-rule scheme without doubling the computational effort. The impact of ε on resolution is illustrated later, in section 3.6.

3.4. The ellipse-shaped trajectory

The second trajectory we considered was an ellipse centered on the origin, with half-axes $A = 360$ mm and $B = 240$ mm. We selected λ as the pseudo-polar angle, so that $\underline{a}(\lambda) = [A\cos\lambda, B\sin\lambda]$ with $\Lambda = [0, 2\pi)$. Consequently, from (27),

$$\begin{cases} \underline{e}_u(\lambda) = \eta(\lambda)[-A\sin\lambda, B\cos\lambda] \\ \underline{e}_w(\lambda) = \eta(\lambda)[B\cos\lambda, A\sin\lambda] \end{cases} \tag{33}$$

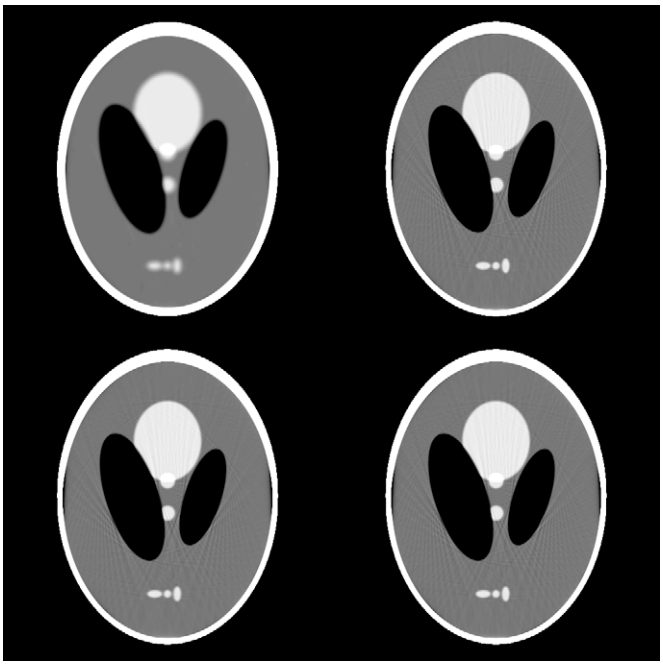

Figure 3. Reconstruction of the Shepp–Logan phantom from fan-beam data on the circular source trajectory. (Top left) The direct scheme. (Top right) The split chain-rule scheme. (Bottom left) The blended chain-rule scheme. (Bottom right) The new scheme with $\varepsilon = 0.001$. The grayscale is compressed on the interval [1.012, 1.032].

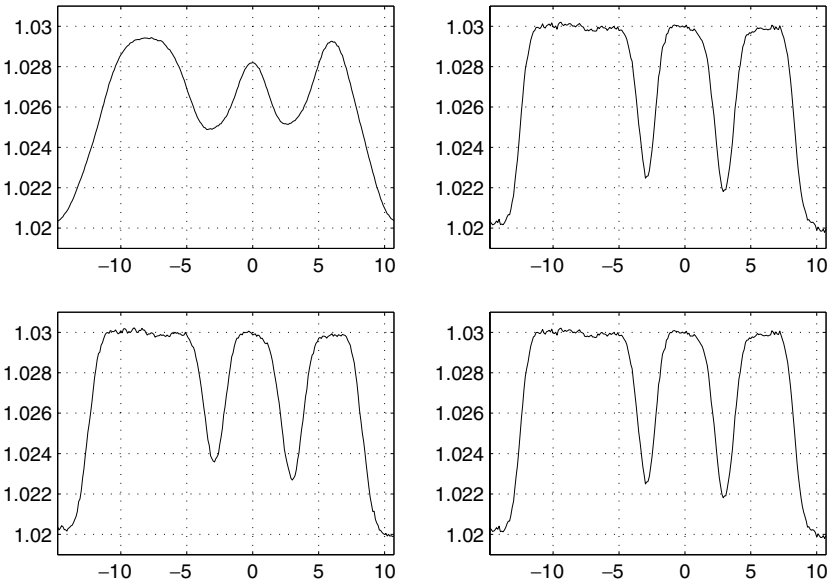

Figure 4. Reconstruction of the Shepp–Logan phantom from fan-beam data on the circular source trajectory. Plot along the line $y = -13$ cm. (Top left) The direct scheme. (Top right) The split chain-rule scheme. (Bottom left) The blended chain-rule scheme. (Bottom right) The new scheme with $\varepsilon = 0.125$.

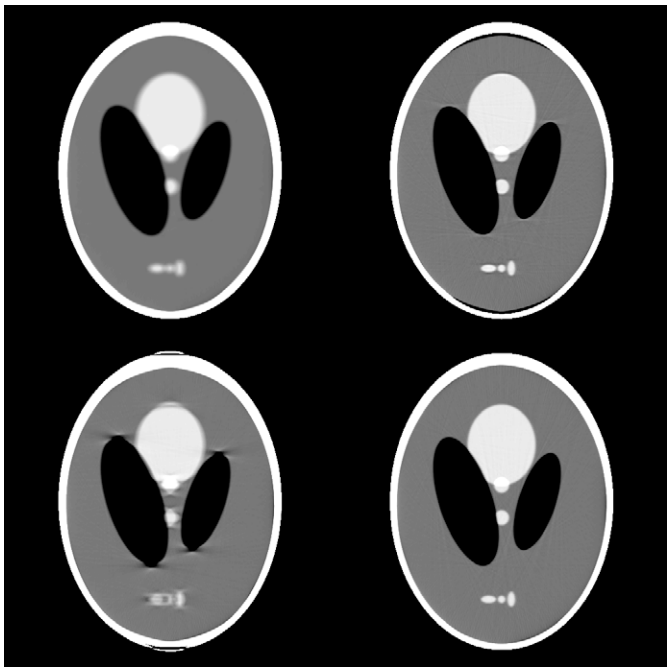

Figure 5. Reconstruction of the Shepp–Logan phantom from fan-beam data on the ellipse-shaped source trajectory. (Top left) The direct scheme. (Top right) The split chain-rule scheme. (Bottom left) The blended chain-rule scheme. (Bottom right) The new scheme with $\varepsilon = 0.125$. The grayscale is compressed on the interval [1.012, 1.032].

and

$$g'_m(\lambda, u) = \left(\frac{\partial g_m}{\partial \lambda}\right)(\lambda, u) + \frac{u^2 + D^2}{D} AB\eta^2(\lambda) \left(\frac{\partial g_m}{\partial u}\right)(\lambda, u), \tag{34}$$

where

$$\eta(\lambda) = 1/\sqrt{A^2 \sin^2 \lambda + B^2 \cos^2 \lambda}. \tag{35}$$

Note that these equations reduce to those for the circle trajectory when substituting R for both A and B.

Testing with this trajectory was performed with the Shepp–Logan phantom, using the same reconstruction grid and the same values for $\Delta\lambda$, Δu and D as for the circular trajectory[4], and using $\varepsilon = 0.125$ for the new scheme. The results are displayed in figures 5 and 6. We observe here that both the direct scheme and the blended chain-rule scheme performs poorly, with the result by the latter being worse due possibly to a problem of resolution differences between the two terms in (34). The split chain-rule scheme performs much better but not as well as the new scheme, as it also suffers some resolution matching problems, as can be seen around the boundaries of each object that form the phantom.

[4] The source–detector distance was thus independent of λ.

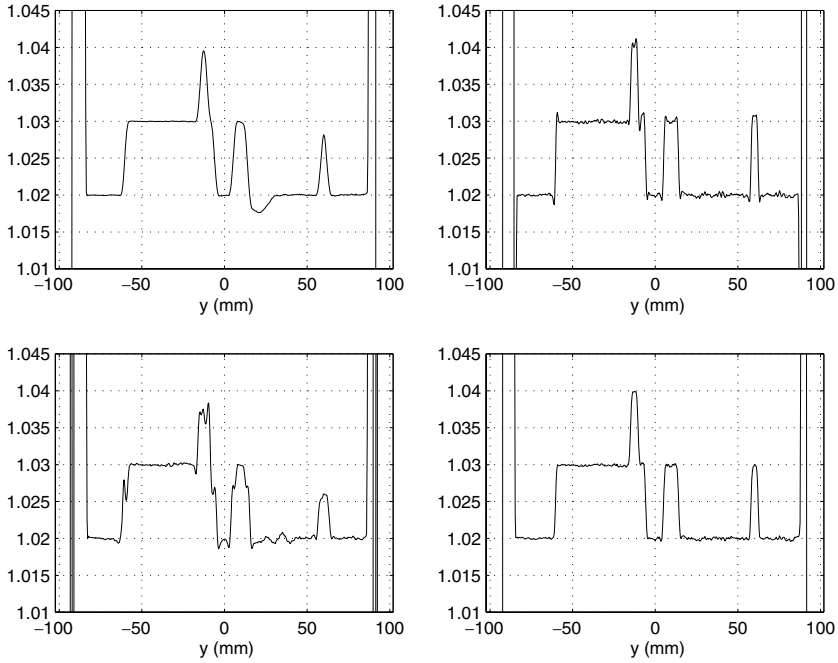

Figure 6. Reconstruction of the Shepp–Logan phantom from fan-beam data on the ellipse-shaped source trajectory. Plot along the line $x = 0$ cm. (Top left) The direct scheme. (Top left) The split chain-rule scheme. (Bottom left) The blended chain-rule scheme. (Bottom right) The new scheme with $\varepsilon = 0.125$.

3.5. The square-shaped trajectory

The third and last trajectory we considered was a square of side $2R = 480$ mm, which we parametrized as follows:

$$\underline{a}(\lambda) = \begin{cases} [R, \lambda - R] & \text{if} \quad \lambda \in [0, 2R) \\ [3R - \lambda, R] & \text{if} \quad \lambda \in [2R, 4R) \\ [-R, 5R - \lambda] & \text{if} \quad \lambda \in [4R, 6R) \\ [\lambda - 7R, -R] & \text{if} \quad \lambda \in [6R, 8R). \end{cases} \tag{36}$$

Thus, λ plays the role of a coordinate along each side of the square, and the source follows this square clockwise with initial position at $[R, -R]$. In this parametrization, vectors $\underline{e}_u(\lambda)$ and $\underline{e}_w(\lambda)$ are independent of λ along each side of the square, so

$$g'_m(\lambda, u) = \left(\frac{\partial g_m}{\partial \lambda}\right)(\lambda, u). \tag{37}$$

Reconstructions using this trajectory were performed using the Shepp–Logan phantom as in the two previous cases. A total of 125 projections uniformly distributed along each side of the square was used with $\Delta u = 1$ mm, $D = 300$ mm and $\varepsilon = 0.125$. Figures 7 and 8 show that in this case the split chain-rule scheme performs poorly compared to the new scheme. Note that, due to the form of (37), the split chain-rule scheme reduces here to the direct scheme, while the blended chain-rule scheme can only perform worse because of the averaging step that is embedded in it.

Figure 7. Reconstruction of the Shepp–Logan phantom from fan-beam data on the square-shaped source trajectory. (Left) The split chain-rule scheme. (Right) The new scheme with $\varepsilon = 0.125$. The grayscale is compressed on the interval [1.012, 1.032].

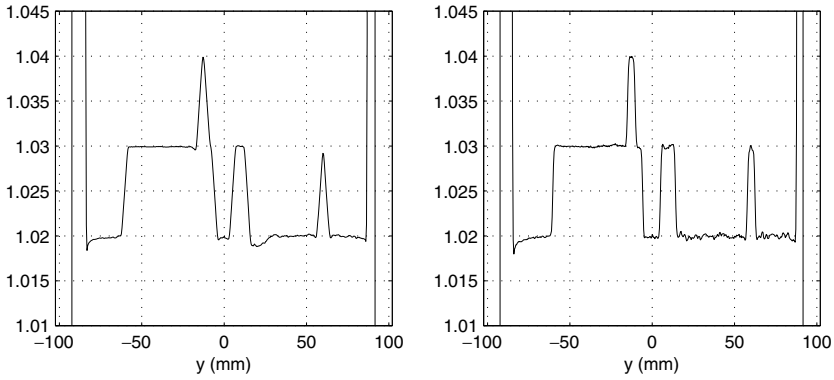

Figure 8. Reconstruction of the Shepp–Logan phantom from fan-beam data on the square-shaped source trajectory. Plot along the line $y = -13$ mm. (Left) The split chain-rule scheme. (Right) The new scheme with $\varepsilon = 0.125$.

3.6. Impact of ε on resolution and noise

In this section, the impact of ε on resolution and noise is illustrated using the FORBILD thorax phantom. We simulated 501 projections of this phantom on the circular trajectory of section 3.3 with $R = 570$ mm, $D = 1040$ mm, $\Delta\lambda = 2\pi/501$ and $\Delta u = 1$ mm. For this simulation, we added the resolution-degradating effects of continuous x-ray emission, anode angle, finite focal spot size and finite detector size, so as to show at the same time that the new scheme is robust to these effects. The focal spot was divided into 3×3 subsources, each detector pixel was divided into 3×3 subpixels, and each projection was obtained through a combination of five subprojections uniformly distributed over the interval $\Delta\lambda$. In total, each value of $g_m(\lambda, u)$ was thus obtained as an (exponential) average of 405 line integrals. The focal spot size was 1.2 cm $\times$ 0.9 cm and the anode angle was 7°.

Reconstructions were performed on a grid of 420×450 square pixels of side 0.5 mm. Since the phantom is almost symmetrical in x, these reconstructions were focused on the region $x \leqslant 0$. Figure 9 shows the results obtained with Poisson noise added to the data, using the new scheme with four different values of ε and also using the direct scheme and the two

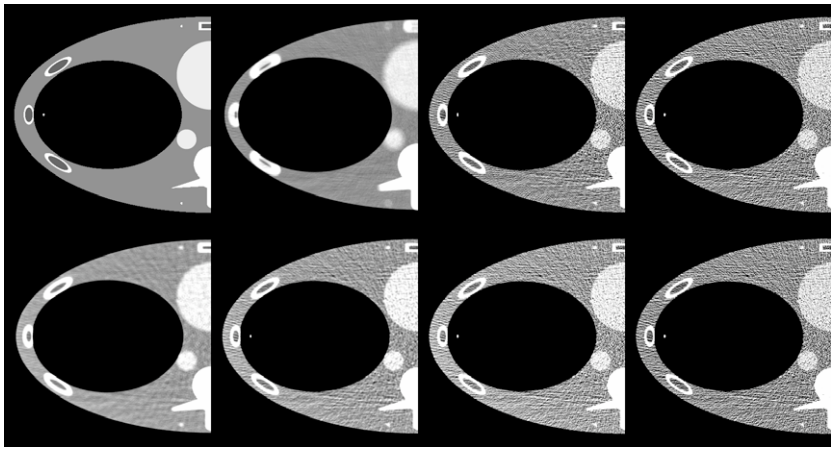

Figure 9. Reconstruction of the FORBILD thorax phantom from noisy fan-beam data on a circular source trajectory. From left to right on the top row: groundtruth and reconstructions with the direct scheme, the blended chain-rule scheme and the split chain-rule scheme. From left to right on the bottom row: reconstructions with the new scheme, using $\varepsilon = 0.24$, $\varepsilon = 0.12$, $\varepsilon = 0.05$ and $\varepsilon = 0.0001$. The grayscale is compressed on the interval $[-60, 60]$ HU.

chain-rule schemes. The four values of ε were 0.24, 0.12, 0.05 and 0.0001. The Poison noise addition was based on an emission of 150 000 photons per ray and a value of 0.0183 mm^{-1} for the tissue attenuation coefficient.

In figure 9, a small bright point can be seen within the lung. This bright point corresponds to a cylinder of diameter 2 mm that was inserted at position $x = -170$ mm and $y = 0$ mm to evaluate resolution. For each differentiation scheme, a noise-free reconstruction focused on this cylinder was performed with a fine pixel size (0.005 mm), so that the full width at half maximum (FWHM) of the cylinder reconstruction could be accurately evaluated in 51 angular directions, which were uniformly distributed over 360°. The mean and the standard deviation of this FWHM over the 51 directions are shown in figure 10 as a function of a noise figure-of-merit that was defined as an ensemble average of the root-mean-squared error in a 2 mm wide annulus region 5 mm away from the cylinder center. The ensemble average was obtained from 30 different noise realizations, using the same noise addition model as for the images in figure 9.

Figures 9 and 10 together show (at least, for this particular study) that (i) the new scheme is robust to resolution-degradating factors, (ii) the new scheme allows significant changes in resolution and noise properties by varying ε, (iii) there exists a threshold value below which reducing ε mostly increases noise without changing resolution, (iv) the new scheme yields a fairly isotropic resolution across the whole range of possible values for ε, (v) the new scheme can perform better than the other three schemes in terms of the chosen noise and resolution figures-of-merit.

Figures 9 and 10 also show that the new scheme allows stable use of small values of ε if desired. However, care must be taken regarding finite numerical machine precision. In this experiment, we observed that using ε smaller than 10^{-9} was not practical. However, differences in image quality were found to be marginal beyond $\varepsilon = 0.0001$. For example, the maximum difference in the pixel values was below 0.33 HU between using $\varepsilon = 0.0001$ and $\varepsilon = 10^{-8}$.

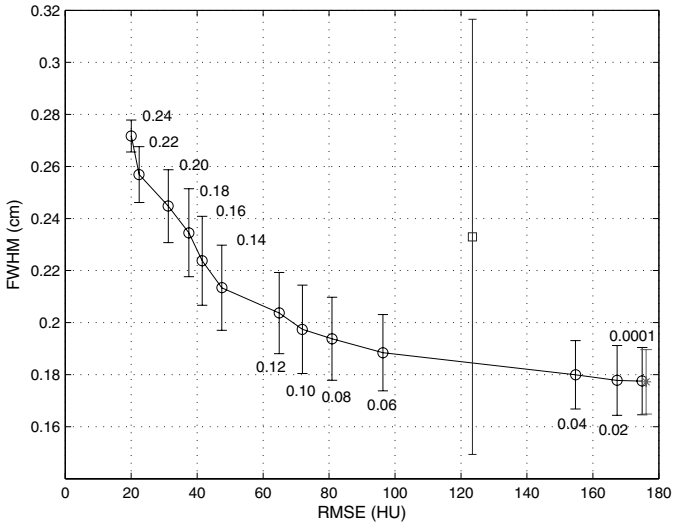

Figure 10. Resolution (FWHM) versus noise (RMSE) for the application of the new scheme with various values of ε (see the circles and the indicated values of ε), for the application of the blended chain-rule scheme (see the square) and for the application of the split chain-rule scheme (see the star). For each point, the standard deviation bars indicate the amount of anisotropy in resolution.

4. Evaluation in cone-beam geometry

We have performed evaluations in CB geometry using the union of two curves for the source trajectory: a circle of radius R and a segment of line attached orthogonally to this circle. This source trajectory was suggested by Zeng and Gullberg (1992) and has been used many times in CB tomography; see e.g., Kudo and Saito (1994), Kudo and Saito (1998), Noo *et al* (1998), Katsevich (2004b) and Johnson *et al* (1998) for some application examples and associated reconstruction algorithms. A single parameter λ could be used to parametrize the source trajectory. However, this would unduly complicate the notation. Hence, we use different parameters to describe each component of the source trajectory: λ_C for the circle and λ_L for the line. In this geometry, it is natural to picture the object as being globally centered on the axis orthogonal to the circle through its center; for application of the new scheme, we selected this axis, which is called the z-axis below, to define the point-of-interest $\underline{b}(\lambda, \underline{\alpha})$ from (26).

4.1. Circle data geometry

The circle was centered on the z-axis in the plane of equation $z = z_0$, and the source position on this circle was denoted as

$$\underline{a}(\lambda_C) = [R\cos\lambda_C, R\sin\lambda_C, z_0] \tag{38}$$

with $\lambda_C \in [0, 2\pi)$. Thus, λ_C is the polar angle in the (x, y)-plane. We assumed $D(\lambda_C)$ was independent of λ_C, and we selected $\underline{e}_u(\lambda_C)$ along the tangent to the circle and $\underline{e}_v(\lambda_C)$ along the z-axis. Hence,

$$\begin{cases} \underline{e}_u(\lambda_C) = [-\sin\lambda_C, \cos\lambda_C, 0] \\ \underline{e}_v(\lambda_C) = [0, 0, 1] \\ \underline{e}_w(\lambda_C) = [\cos\lambda_C, \sin\lambda_C, 0]. \end{cases} \tag{39}$$

For this particular geometry, the data are $g_m(\lambda_C, u, v)$, and from equations (15) and (39)

$$g'_m(\lambda_C, u, v) = \left(\frac{\partial g_m}{\partial \lambda_C}\right)(\lambda_C, u, v) + \frac{u^2 + D^2}{D}\left(\frac{\partial g_m}{\partial u}\right)(\lambda_C, u, v) + \frac{uv}{D}\left(\frac{\partial g_m}{\partial v}\right)(\lambda_C, u, v). \tag{40}$$

4.2. Line data geometry

The line segment intersects the circle at $\underline{x} = [-R, 0, z_0]$ and the source position on this line segment was denoted as

$$\underline{a}(\lambda_L) = [-R, 0, \lambda_L] \tag{41}$$

with $\lambda_L \in [z_B, z_T]$. Thus, λ_L is a Cartesian coordinate, and the z-extent of the line segment is controlled by two parameters, z_B and z_T, that give the z coordinate of the first and the last source positions on it.

The distance $D(\lambda_L)$ was assumed to be independent of λ_L, as in the circle case. Also, we selected $\underline{e}_u(\lambda_L)$ and $\underline{e}_v(\lambda_L)$ to be identical to the expression of vectors $\underline{e}_u(\lambda_C)$ and $\underline{e}_v(\lambda_C)$ at $\lambda_C = \pi$. Thus,

$$\begin{cases} \underline{e}_u(\lambda_L) = [0, -1, 0] \\ \underline{e}_v(\lambda_L) = [0, 0, 1] \\ \underline{e}_w(\lambda_L) = [-1, 0, 0]. \end{cases} \tag{42}$$

In this geometry, the data on the line segment are $g_m(\lambda_L, u, v)$, and from equations (15) and (42)

$$g'_m(\lambda_L, u, v) = \left(\frac{\partial g_m}{\partial \lambda_L}\right)(\lambda_L, u, v). \tag{43}$$

Observe that in our notation there is no way to know if $\underline{a}(0)$ is a point on the circle or the line. To avoid this ambiguity, an index L could be attached to $g'_m(\lambda_L, u, v)$ and $\underline{a}(\lambda_L)$, thus writing for example $\underline{a}^L(\lambda_L)$ instead of $\underline{a}(\lambda_L)$ for the source position on the line. However, since we never need to discuss the data or the source position at a specific λ_L, we omit this notation burden. Hereafter, if λ_L is seen as a variable of some function, it should be understood that this function refers to the line data, and the same with λ_C.

4.3. The reconstruction formula

For reconstruction, we decided to apply the general reconstruction scheme of Katsevich (2003), using the weighting function Kudo and Saito suggested in Kudo and Saito (1994) and Kudo and Saito (1998) for handling the redundancies in the 3D Radon domain. This approach provides a theoretically-exact reconstruction technique that combines the efficiency of Katsevich's scheme to Kudo and Saito's allowance of truncation in v, thus permitting accurate reconstruction of a portion of a long object in z with x-ray exposure mostly limited to this portion.

The reconstruction formula we obtained yields a regularized version $\hat{f}(\underline{x})$ of $f(\underline{x})$ according to the following equation:

$$\hat{f}(\underline{x}) = \frac{1}{4\pi}\int_0^{2\pi} \frac{g_F(\lambda_C, u^*(\lambda_C, \underline{x}), v^*(\lambda_C, \underline{x}))}{R - \underline{x}\cdot\underline{e}_w(\lambda_C)}\, d\lambda_C + \frac{1}{4\pi D}\int_{z_B}^{z_T} \frac{g_F(\lambda_L, u^*(\lambda_L, \underline{x}), v^*(\lambda_L, \underline{x}))}{R - \underline{x}\cdot\underline{e}_w(\lambda_L)}\, d\lambda_L \tag{44}$$

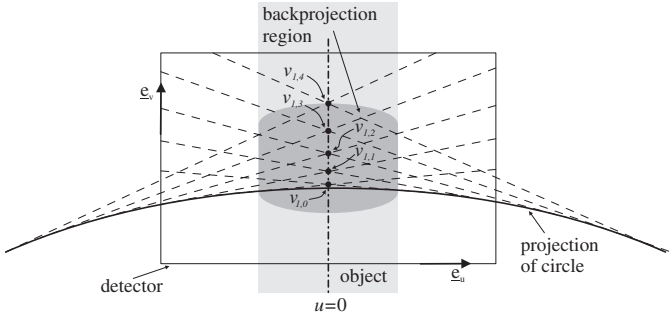

Figure 11. Filtering lines for a source position along the line segment of the CB trajectory in section 4. These lines are tangent to the projection of the circle and parametrized by their intersection v_1 with the axis $u = 0$ and by the sign e of their slope (see section 4.3). Five filtering lines are illustrated here for both $e = 1$ and $e = -1$.

where

$$u^*(\lambda_C, \underline{x}) = -D\frac{(\underline{x} - \underline{a}(\lambda_C)) \cdot \underline{e}_u(\lambda_C)}{(\underline{x} - \underline{a}(\lambda_C)) \cdot \underline{e}_w(\lambda_C)} \tag{45}$$

and

$$v^*(\lambda_C, \underline{x}) = -D\frac{(\underline{x} - \underline{a}(\lambda_C)) \cdot \underline{e}_v(\lambda_C)}{(\underline{x} - \underline{a}(\lambda_C)) \cdot \underline{e}_w(\lambda_C)}, \tag{46}$$

while $u^*(\lambda_L, \underline{x})$ and $v^*(\lambda_L, \underline{x})$ are obtained through substitution of λ_L for λ_C in these expressions.

The filtered circle data, $g_F(\lambda_C, u, v)$, in equation (44) are given by

$$g_F(\lambda_C, u, v) = \int_{-\infty}^{\infty} du\, h_H\left(u^*(\lambda, \underline{x}) - u\right) \frac{Dg'_m(\lambda_C, u, v)}{\sqrt{D^2 + u^2 + v^2}}, \tag{47}$$

where $h_H(u)$ is the Hilbert filter given in (31). Comparing equations (44) and (47) together with formula (29), which was given in section 3.2 for fan-beam reconstruction, the first term in (44) appears clearly as a 3D extension of (29) following the principles of the FDK algorithm (Feldkamp *et al* 1984). Note that this extension was suggested by Yu and Wang (2004).

The filtered line data, $g_F(\lambda_L, u, v)$, in equation (44) may be described in various ways. Here, we give a step-by-step description that is somewhat lengthy but reflects our implementation.

Step 1. Apply a length-correction factor to get

$$g_W(\lambda_L, u, v) = \frac{Dg'_m(\lambda_L, u, v)}{\sqrt{u^2 + v^2 + D^2}}. \tag{48}$$

Step 2. Apply a Hilbert transform along lines in the detector plane that are tangent to the projection of the circle component of the source trajectory. These filtering lines can be parametrized by their intersection v_1 with the axis $u = 0$; see figure 11. The result of this step is

$$g_T(\lambda_L, u, v_1, e) = \int_{-\infty}^{\infty} h_H(u - u') g_W(\lambda_L, u', v_1 + cu')\, du' \tag{49}$$

with

$$c = e\frac{2}{D}\sqrt{\eta(v_1 + \eta)}, \qquad \eta = \frac{D}{2R}(\lambda_L - z_0). \tag{50}$$

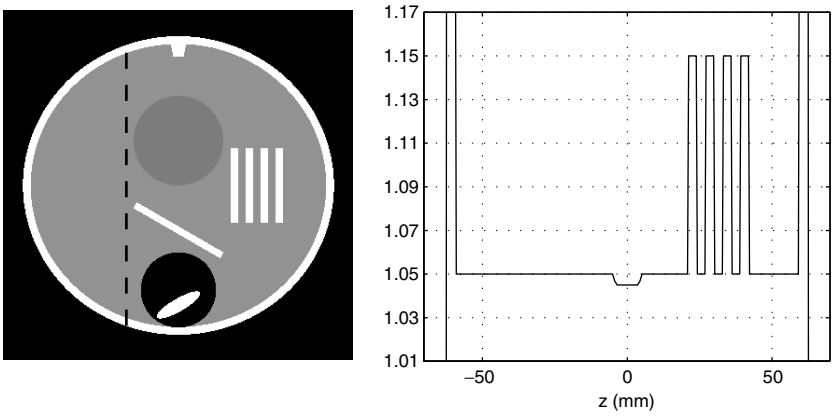

Figure 12. Cone-beam reconstruction is tested using a version of FORBILD head phantom with no ears and added disks. (Left) Slice $x = 0.0$ mm through the phantom; the z-axis is horizontal and the broken vertical line indicates the position of the circle scan. (Right) Plot along the line $y = -0.1875$ mm through the slice displayed on the left.

In this expression, e is meant to take only two values: $+1$ and -1. The value of e defines thus the sign of the slope of the tangent line along which filtering is performed. Equation (49) applies to any value of v_1 such that $\eta(v_1 + \eta) \geqslant 0$.

Step 3. Obtain $g_{\mathrm{F}}(\lambda_{\mathrm{L}}, u, v)$ as the difference of Hilbert transforms of $g_W(\lambda_{\mathrm{L}}, u, v)$ along the two lines that are tangent to the projection of the circle through (u, v):

if $v/\eta > -(1 + u^2/D^2)$

$$g_{\mathrm{F}}(\lambda_{\mathrm{L}}, u, v) = g_{\mathrm{T}}\left(\lambda_{\mathrm{L}}, u, v - c_+ u, \frac{c_+}{|c_+|}\right) - g_{\mathrm{T}}\left(\lambda_{\mathrm{L}}, u, v - c_- u, \frac{c_-}{|c_-|}\right) \tag{51}$$

else $\quad g_{\mathrm{F}}(\lambda_{\mathrm{L}}, u, v) = 0$

where

$$c_\pm = -\frac{2\eta}{D^2}u \pm \frac{2}{D}\sqrt{\frac{\eta^2}{D^2}u^2 + \eta(v + \eta)}. \tag{52}$$

Note that variable e in g_{T} allows accounting for the fact that the two tangent lines through (u, v) are not always of opposite slope sign, that is c_+ and c_- can have the same sign or opposite signs depending on the specific value of (u, v).

As in the fan-beam case, $\hat{f}(\underline{x})$ converges toward $f(\underline{x})$ in L^2 norm when Δu converges toward zero and $f(\underline{x})$ is a square-integrable function.

The implementation of (49) was performed using linear interpolation in v followed by an FFT-based convolution, the computation of g_{F} from g_{T} in (51) was performed using bilinear interpolation, and the backprojection integral in (44) was implemented using the trapezoidal rule with bilinear interpolation in (u, v). Also, the variable v_1 in g_{T} was sampled with a step Δv, and the FFT-based convolution was applied with a half-pixel shift.

4.4. Results

The reconstruction formula was tested on CB data of the FORBILD head phantom with no ears, to which we added four disks of height 6 mm, diameter 60 mm, and centered on the z-axis at $z = 45, 57, 69, 81$ mm. There was thus a gap of 6 mm separating any two successive disks. Figure 12 shows the slice $x = 0$ through the phantom and a profile through this slice.

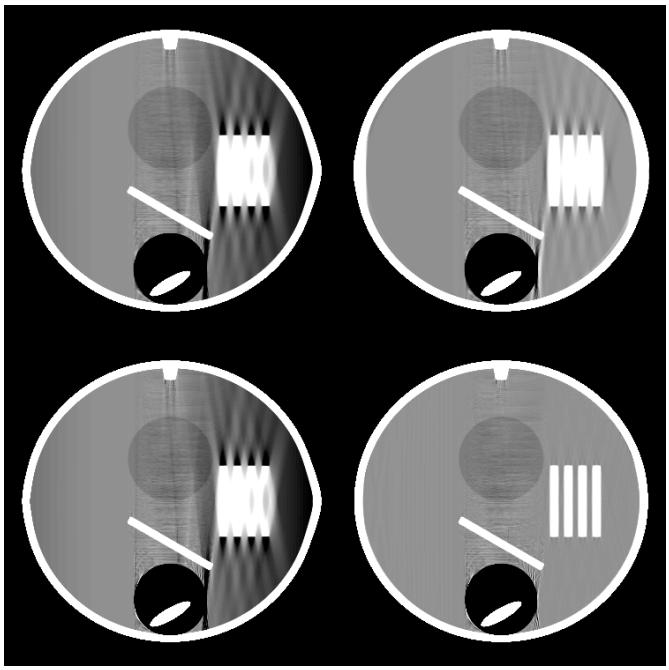

Figure 13. Reconstruction of slice $x = 0$ mm through the FORBILD head phantom with added disks and no ears. In these images, the z-axis is horizontal. (Top row) Reconstructions using the split chain-rule scheme. (Bottom row) Reconstructions using the new scheme with $\varepsilon = 0.0001$. In each case, the left image is the result from using the circle-scan data only, while the right image corresponds to using both the circle-scan and the line-scan data. The grayscale is compressed on the interval [1.02, 1.08].

The circle was placed in the plane $z = -40$ mm, and the circle data were simulated for 1160 source positions with $\Delta\lambda_C = 2\pi/1160$ and $R = 570$ mm. The line data were simulated for 85 source positions, starting at $z_B = -290$ mm with $\Delta\lambda_L = 8$ mm. In each case, the detector grid was defined with $\Delta u = \Delta v = 1.5$ mm.

Figures 13 and 14 illustrate the performance of using the new scheme against that of using the split chain-rule scheme. The high sampling in λ_C was chosen so that little difference in the contribution from circle data (the first term in (44)) could be expected between the two schemes, and all major differences in final image quality could be attributed to processing the line data. Clearly, the new scheme was much better at taking advantage of the line scan data to remove the artifacts in the reconstruction from the circle data, even though the sampling step on the line was larger than the distance between the disks.

5. Discussion and conclusion

We have developed a new scheme to perform the view-dependent differentiation that must be applied to the data in various analytical reconstruction algorithms in FB and CB tomography. This scheme was tested against two other published schemes in a number of scenarios. The test demonstrated a strong robustness to variations in data acquisition geometry and view

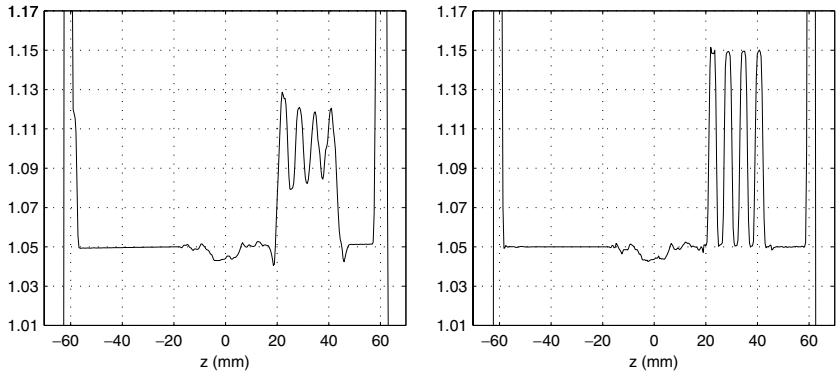

Figure 14. Plots along the line $y = -0.1875$ mm through slice $x = 0$ mm of the reconstructions from circle-plus-line CB data shown in figure 12. (Left) Using the split chain-rule scheme. (Right) Using the new scheme with $\varepsilon = 0.0001$.

sampling, unlike for the other two schemes. The test also demonstrated that the new scheme is stable in the presence of data noise.

We make no claim that our new scheme is optimal, as we could only compare its performance to a limited number of alternative schemes. However, at limited computational effort, the new scheme seems highly competitive. The ability to adjust resolution through the selection of parameter ε is furthermore an attractive feature that has not been seen in other schemes.

It could be argued for the fan-beam experiments with the ellipse and the square that the definition of the data with coordinate $u = 0$ at the orthogonal projection of the source onto the detector plane is not practical, and that better results could be obtained with the chain-rule scheme if the origin $u = 0$ was selected along the line that connects the source position to the origin. This could be possible and was not tested. However, the important point is that the new scheme is robust to this issue; the new scheme does not require a parametrization of data that fits best the needs of the differentiation step. Furthermore, in the circle-and-line CB geometry, our choice for the origin of (u, v) is reasonable. The independence of the new scheme on changes in geometry from one source position to another is important for C-arm imaging, as discussed in Hoppe *et al* (2006).

As we have seen, the new scheme relies on a specific definition for the point-of-interest $\underline{b}(\lambda, \underline{\alpha})$. For large objects relative to the source trajectory, it could be advantageous to split the object into a number of contiguous regions and use different definitions of $\underline{b}$ for each of these regions. However, at this stage, we have not met any case where doing so appeared to be needed. Furthermore, it is tempting to think the new scheme would perform even better if the implementation involved shifting the position of the projections by $(\Delta\lambda)/2$. This option was tested and was found to provide no additional gain.

Performance in resolution using the new scheme against the alternative of using integration by parts (Katsevich (2002), Chen (2003b), Katsevich *et al* (2006), Yang *et al* (2006)) was not evaluated. It could be that integration by parts still allows reconstruction with higher resolution. However, we believe that any difference is most likely marginal. This topic is currently under investigation.

The CB reconstruction example gives a warning in terms of unduly blaming projection sampling for limited resolution in the reconstruction, as the sampling along the line segment

($\Delta\lambda_L = 8$ mm) could have easily been argued to be too coarse to resolve the disks, which had a thickness of 6 mm and were separated from each other by gaps of 6 mm. In fact, it was the chain-rule scheme that was deficient in taking advantage of the given sampling conditions.

To our knowledge, the reconstruction algorithm we suggested for circle-plus-line CB reconstruction is original. However, as explained, its derivation is straightforward from results by Kudo and Saito (1994, 1998), and by Katsevich (2003). The experiment results we obtained from computer-simulated data appeared quite good when using the new scheme for data differentiation, and it will be interesting to see in the future this algorithm in action on real data.

References

Bontus C, Köhler T and Proksa R 2005 EnPiT: filtered back-projection algorithm for helical CT using an n-Pi acquisition *IEEE Trans. Med. Imaging* **24** 977–86

Chen G H 2003a An alternative derivation of Katsevich's cone-beam reconstruction formula *Med. Phys.* **30** 3217–26

Chen G H 2003b A new framework of image reconstruction from fan beam projections *Med. Phys.* **30** 1151–61

Feldkamp L A, Davis L C and Kress J W 1984 Practical cone-beam algorithm *J. Opt. Soc. Am.* A **1** 612–9

Hoppe S, Dennerlein F, Lauritsch G, Hornegger J and Noo F 2007 Cone-beam tomography from short-scan circle-plus-arc data measured on a C-arm system *Conf. Record of the 2006 IEEE Nuclear Science Symp. and Medical Imaging Conf. (San Diego, CA, USA)*

Johnson R H, Hu H, Haworth S T, Cho P S, Dawson C A and Linehan J H 1998 Feldkamp and circle-and-line cone-beam reconstruction for 3D micro-CT of vascular networks *Phys. Med. Biol.* **43** 929–40

Johnson L W and Riess R D 1982 *Numerical Analysis* 2nd edn (Reading, MA: Addison-Wesley)

Kak A C and Slaney M 1988 *Principles of Computerized Tomographic Imaging* (Piscataway, NJ: IEEE)

Katsevich A 2002 Analysis of an exact inversion algorithm for spiral cone-beam CT *Phys. Med. Biol.* **47** 2583–97

Katsevich A 2003 A general scheme for constructing inversion algorithms for cone–beam CT *Int. J. Math. Math. Sci.* **21** 1305–21

Katsevich A 2004a An improved exact filtered backprojection algorithm for spiral computed tomography *Adv. Appl. Math.* **32** 681–97

Katsevich A 2004b Image reconstruction for the circle and line trajectory *Phys. Med. Biol.* **49** 5059–72

Katsevich A, Lauritsch G, Bruder H, Flohr T and Stierstorfer K 2003 Evaluation and empirical analysis of an exact FBP algorithm for spiral cone-beam CT *SPIE Med. Imaging 2003* **5032** 663–74

Katsevich A, Taguchi K and Zamyatin A A 2006 Formulation of four Katsevich algorithms in native geometry *IEEE Trans. Med. Imaging* **25** 855–68

Kudo H and Saito T 1994 An extended completeness condition for exact cone-beam reconstruction and its application *Nucl. Sci. Symp. and Medical Imaging Conf. (Norfolk, VA, USA)* vol 4 pp 1710–4

Kudo H and Saito T 1998 Fast and stable cone-beam filtered backprojection method for non-planar orbits *Phys. Med. Biol.* **43** 747–60

Noo F, Defrise M and Clack R 1998 Direct reconstruction of cone-beam data acquired with a vertex path containing a circle *IEEE Trans. Image Process.* **7** 854–67

Noo F, Defrise M, Clackdoyle R and Kudo H 2002 Image reconstruction from fan-beam projections on less than a short scan *Phys. Med. Biol.* **47** 2525–46

Noo F, Pack J D and Heuscher D 2003 Exact helical reconstruction using native cone–beam geometries *Phys. Med. Biol.* **48** 3787–818

Pack J D and Noo F 2005 Cone-beam reconstruction outside *R*-lines using the backprojection of 1-D filtered data *Proc 8th Int. Meeting on Fully Three-dimensional Image Reconstruction in Radiology and Nuclear Medicine (Salt Lake City, UT)* ed F Noo, G L Zeng and H Kudo pp 287–90 http://www.ucair.med.utah.edu/3D05/proceedings.html

Sidky E Y, Zou Y and Pan X 2005 Minimum data image reconstruction algorithms with shift-invariant filtering for helical, cone-beam CT *Phys. Med. Biol.* **50** 1643–57

Yang H, Li M, Koizumi K and Kudo H 2006 View-independent reconstruction algorithms for cone beam CT with general saddle trajectory *Phys. Med. Biol.* **51** 3865–84

Ye Y and Wang G 2005 Filtered backprojection formula for exact image reconstruction from cone-beam data along a general scanning curve *Med. Phys.* **32** 42–8

Ye Y, Zhao S, Yu H and Wang G 2005 A general exact reconstruction for cone-beam CT via backprojection-filtration *IEEE Trans. Med. Imaging* **24** 1190–8

Yu H and Wang G 2004 Feldkamp-type VOI reconstruction from super-short-scan cone-beam data *Med. Phys.* **31** 1357–62

Yu H, Ye Y, Zhao S and Wang G 2005 A backprojection-filtration algorithm for nonstandard spiral cone-beam CT with an n-PI-window *Phys. Med. Biol.* **50** 2099–111

Zeng G L and Gullberg G T 1992 A cone-beam tomography algorithm for orthogonal circle-and-line orbit *Phys. Med. Biol.* **37** 563–77

Zou Y and Pan X 2004 Exact image reconstruction on PI-lines from minimum data in helical cone-beam CT *Phys. Med. Biol.* **49** 941–59